Materials & Design 271 (2026) 117160

Contents lists available at ScienceDirect

Materials & Design

journal homepage: www.elsevier.com/locate/matdes

Machine learning-driven multi-objective optimisation of shape-memory programming parameters in 4D-printed PLA

Ayhan Hacıoğlu [a,*], Meltem Eryildiz [b], Erkan Caner Ozkat [a]

[a] Department of Mechanical Engineering, Faculty of Engineering and Architecture, Recep Tayyip Erdogan University, 53100 Rize, Turkey
[b] Department of Mechanical Engineering, Faculty of Engineering and Architecture, Istanbul Beykent University, Istanbul, Turkey

ARTICLE INFO

Keywords:
Additive manufacturing
4D printing
Shape-memory polymer
Multi-objective optimisation
Design of experiments
Machine learning surrogate model

ABSTRACT

4D printing extends additive manufacturing by introducing time-dependent functionality through stimuli-responsive feedstocks such as shape-memory polymers (SMPs). In 4D-printed PLA, performance is governed by programming temperature, holding time, and recovery temperature, whose effects are reflected in recovery time, shape fixity ratio, and shape recovery ratio. This study combines a replicated 49-condition Latin-square design, machine-learning surrogate models, NSGA-II multi-objective optimisation, and experimental validation to identify a Pareto-optimal process window. Eight regression models were evaluated using leave-one-condition-out (LOCO) cross-validation with nested hyperparameter selection. The surrogates achieved LOCO R^2 values of 0.973 (RMSE 7.29 s) for recovery time, 0.874 (1.17 percentage points, pp) for the shape fixity ratio, and 0.975 (4.31 pp) for the shape recovery ratio. The shape fixity ratio increased from 90.2% to 98.8% between 50 and 55 °C before plateauing, with no significant additional effect of holding time. NSGA-II identified a knee point at 67.5 °C programming temperature, 2.0 min holding time, and 80.0 °C recovery temperature, predicting a recovery time of 3.14 s, shape fixity ratio of 99.72%, and shape recovery ratio of 91.70%. Across five validation points, maximum absolute deviations were 0.36 s, 0.75 pp, and 3.82 pp for recovery time, shape fixity ratio, and shape recovery ratio.

1. Introduction

Shape-memory materials are active materials that can be deformed into a temporary configuration and subsequently recover a predefined permanent shape when exposed to an external stimulus. Although shape-memory behaviour was among the earliest and most widely demonstrated in metallic alloy systems such as Au-Cd and TiNi [1,2], shape-memory polymers (SMPs) have attracted increasing attention owing to their low density, large recoverable strain, ease of processing, and tunable transition or activation temperatures [3,4]. Among the various possible stimuli, thermal activation remains one of the most widely used routes because it exploits temperature-dependent polymer mobility associated with the glass transition or melting transition and is compatible with many thermoplastic polymers used in additive manufacturing [5,6].

Additive manufacturing has expanded the potential of SMPs by enabling programmable shape change to be designed not only through material chemistry, but also through geometry, architecture, printing strategy, and spatial material distribution. This concept forms the basis of 4D printing, where the fourth dimension refers to the time-dependent change in the shape, properties, or function of a printed object after exposure to an external stimulus [7,8]. Beyond its conceptual novelty, 4D printing is increasingly being explored across biomedical and healthcare devices, soft robotics, aerospace and automotive systems, smart textiles and wearable technologies, sensors, and other adaptive structures whose geometry, properties, or function are designed to evolve after fabrication or deployment [7,8]. These application demands place particular emphasis on predictable actuation, reliable temporary-shape fixation, and repeatable recovery, making the control of thermally activated SMP behaviour a central issue. In material-extrusion-based systems, fused filament fabrication (FFF) provides such a practical route for polymer-based 4D printing because it uses thermoplastic filament feedstocks, relatively low-cost and accessible equipment, and digitally controlled material deposition [9,10].

In FFF-based 4D printing, the functional response is not governed by material selection alone. Printing-related variables, material formulation, infill or lattice architecture, and post-printing programming conditions can all affect recovery behaviour and overall shape-memory

* Corresponding author.
E-mail address: ayhan.hacioglu@erdogan.edu.tr (A. Hacıoğlu).

https://doi.org/10.1016/j.matdes.2026.117160
Received 5 August 2026; Received in revised form 13 September 2026; Accepted 28 September 2026
Available online 29 September 2026
0264-1275/© 2026 The Author(s). Published by Elsevier Ltd. This is an open access article under the CC BY license (http://creativecommons.org/licenses/by/4.0/).

performance [11–13]. This is because the printed polymer is not merely a passive material system, but a programmable structure whose response depends on its thermomechanical programming and recovery history [11,14].

Among these factors, the post-printing thermomechanical programming/recovery cycle plays a particularly decisive role in determining the functional performance of thermally activated SMPs. During this cycle, the polymer is deformed above or near its characteristic thermal transition, where temperature-dependent molecular mobility is governed by the glass-transition or melting region. The temporary shape is then fixed by cooling below this transition range, and recovery is subsequently triggered by reheating into the thermally activated mobility region [14,15]. Within this framework, programming and thermal activation conditions can markedly influence shape fixity and recovery [15], while holding time has also been reported to affect shape fixity during programming [16]. These observations motivate treating the programming/recovery cycle as a process-response mapping problem in which multiple inputs and multiple functional outputs are analysed together.

Data-driven surrogate modelling provides a suitable framework for addressing this need because it can approximate complex process-response relationships from structured data and can be coupled with optimisation algorithms to explore feasible process windows computationally [17]. Its broader applicability in engineering is also demonstrated by classification and anomaly-detection studies across manufacturing, geotechnical, and sensor-based applications [18–21]. Further examples of machine-learning applications in engineering include optimisation-assisted neural networks, ensemble learning, constrained neural networks, and tree-based approaches [22–25]. In polymer additive manufacturing, these approaches are increasingly used to model interdependencies among material composition, printing parameters, thermal conditions, microstructural features, and post-processing conditions, thereby supporting materials design, process-parameter optimisation, property prediction, and decision support [26,27]. For 4D printing, however, the modelling task is more demanding because the target response is not a single material property, but a time-dependent shape transformation governed by printing, programming, and recovery conditions.

Recent studies have also applied machine-learning-assisted and reinforcement-learning-based inverse-design strategies to predict or generate target shape transformations in programmable structures [28,29]. However, their main focus remains on material distribution, target-shape generation, or structural inverse design, whereas the offline selection of post-printing programming/recovery conditions remains less explored. Such selection requires simultaneous consideration of multiple experimentally measured functional responses.

Multi-objective optimisation is therefore important because recovery kinetics, temporary-shape retention, and final shape recovery may respond differently to programming and recovery conditions. A useful programming cycle should balance fast recovery, reliable temporary-shape fixation, and high final recovery rather than maximising a single response. When programming temperature, holding time, and recovery temperature are varied simultaneously, these competing responses can define an operating window that cannot be reliably identified through isolated parameter comparisons.

Although post-printing programming and recovery conditions have been investigated in thermally activated 4D-printed polymers, previous studies have generally focused on predefined thermomechanical protocols, selected parameter sets, or material-specific performance assessments [30–34]. These approaches provide useful insights but do not fully represent the programming/recovery cycle as a statistically structured multi-factor process window. Moreover, replicated experiments contain within-condition variability that should be considered during surrogate-model development and evaluation [35,36]. Thus, a gap remains for a replicate-informed, surrogate-assisted framework that can jointly characterise the thermomechanical programming/recovery process and support multi-objective selection of operating conditions.

The present study addresses this gap by developing an experimentally replicated multi-objective process-window framework for the post-printing thermomechanical programming/recovery cycle of 4D-printed PLA. A statistically structured experimental design is combined with condition-grouped nested cross-validation to characterise process-response relationships and evaluate surrogate-model performance. The causal sequence of the shape-memory cycle is incorporated by treating shape fixity as a programming-stage response, independent of the subsequent recovery temperature. The selected surrogate models are then coupled with the Non-dominated Sorting Genetic Algorithm II (NSGA-II) optimisation to identify Pareto-optimal programming/recovery conditions, which are assessed through replicate validation experiments. The framework provides a process-window-based understanding of how programming and recovery conditions jointly govern recovery time, temporary-shape retention, and final shape recovery, strengthening the methodological basis for optimisation of the thermomechanical operating window of 4D-printed PLA.

The remainder of the paper is organised as follows: Section 2 presents the experimental and computational methodology, Section 3 reports the results and validation, Section 4 discusses the findings and their implications, and Section 5 summarises the main conclusions and future directions.

2. Materials and methods

2.1. Material

Commercial transparent poly(lactic acid) (PLA) filament, 4043D grade, supplied by Filameon (Kayseri, Türkiye), was used as the thermally responsive polymeric material in this study. PLA was selected due to its processability by fused filament fabrication and its ability to exhibit thermally activated shape-memory behaviour under suitable programming and recovery conditions. The glass transition temperature (T_g) of the investigated PLA was determined by differential scanning calorimetry (DSC) to be within the range of approximately 55–65 °C, and the corresponding thermogram (Fig. S1) is provided in the Supplementary Material.

2.2. Fabrication of PLA samples

The PLA samples were fabricated using a Bambu Lab X1E 3D printer. The slicing process was carried out using Bambu Studio v.2.5.0.66. A textured polyetherimide (PEI) build plate and a 0.4 mm nozzle were used for all prints. In order to minimise the influence of printing-related variations on the shape-memory response, the printing parameters were kept constant for all samples.

The nozzle temperature and bed temperature were set to 210 °C and 45 °C, respectively. The layer height was set to 0.20 mm. Rectangular strip specimens with dimensions of 80 × 8 × 1.5 mm were printed at 100% infill density using an aligned rectilinear infill pattern oriented at 0°. The printing speed was kept at 50 mm/s. Wall loops and top/bottom shells were set to zero in accordance with the selected slicing configuration.

2.3. Shape-memory programming and recovery procedure

The shape-memory behaviour of the printed PLA samples was evaluated using a thermally activated bending-recovery procedure (Fig. 1). Initially, each sample was considered to be in its original permanent shape, corresponding to an initial angle of $\theta_0 = 180^{\circ}$. During the programming step, the samples were heated to the selected programming temperature, T_p, and held at this temperature for the prescribed holding time, t_{hold}. The softened samples were then bent to a programmed angle of $\theta_p = 90^{\circ}$ using a fixed-angle guide. While maintaining the applied

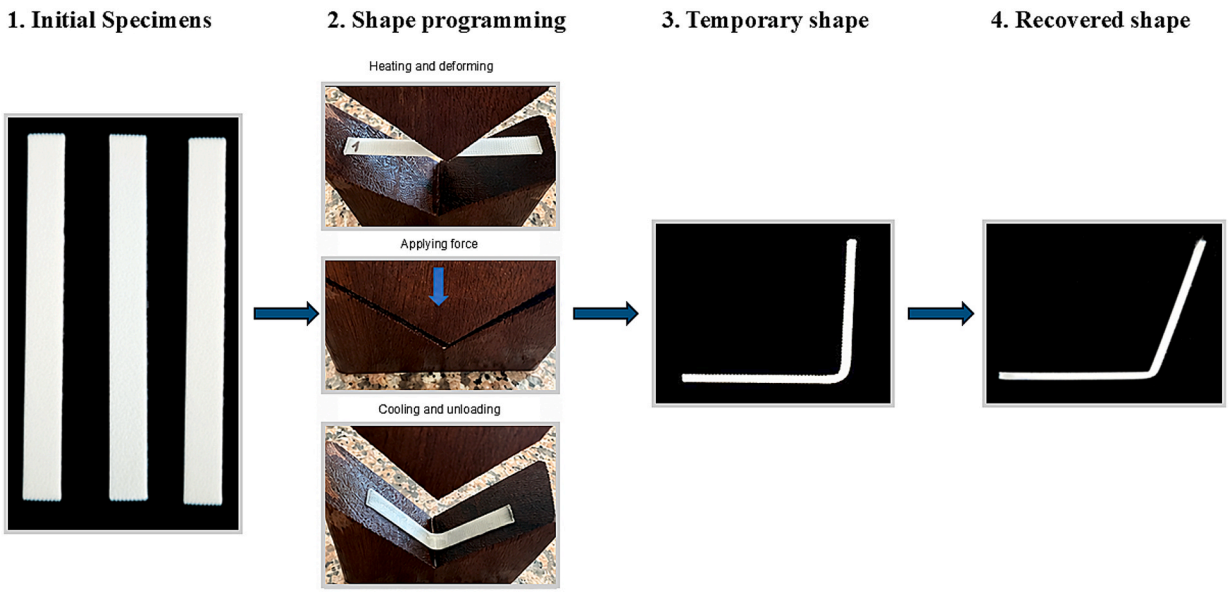


Fig. 1. Shape-memory testing procedure of the FFF-printed PLA samples, showing the initial, programmed temporary, and recovered shapes.

deformation, the samples were cooled down to room temperature in order to fix the temporary shape. After complete cooling, the external constraint was removed, and the angle after unloading was recorded as θ_u.

The recovery step was performed by immersing the programmed samples in a hot-water bath maintained at the selected recovery temperature, T_r. The recovery process was monitored until no further visible angular change occurred. The time required to reach the stable recovered shape was recorded as the recovery time, t_{rec}, and the final recovered angle was recorded as θ_r. The intermediate and final angles were recorded photographically and measured using ImageJ software.

The shape fixity ratio (R_f) and shape recovery ratio (R_r) were calculated using the following equations:

$$R_f(\%) = \frac{\theta_0 - \theta_u}{\theta_0 - \theta_p} \times 100$$
$$R_r(\%) = \frac{\theta_r - \theta_u}{\theta_0 - \theta_u} \times 100 \quad (1)$$

where θ_0 is the initial angle, θ_p is the programmed angle, θ_u is the angle measured after unloading, and θ_r is the final angle measured after thermal recovery. A higher R_f value indicates better retention of the programmed temporary shape, whereas a higher R_r value indicates greater recovery toward the original permanent shape. Since θ_u, and hence the shape fixity ratio, is measured before the recovery step, shape fixity is governed only by the programming stage. Therefore, T_p and t_{hold} are used as the only inputs in the statistical and surrogate models for shape fixity.

2.4. Experimental design and dataset

The dataset used in this study consisted of 147 measurements obtained from 49 distinct experimental conditions over three thermo-mechanical process factors: the programming temperature, $T_p \in \{50, 55, 60, 65, 70, 75, 80\}$ °C, the holding time at the programming temperature, $t_{hold} \in \{2, 3, 4, 5, 6, 7, 8\}$ min, and the recovery temperature, $T_r \in \{50, 55, 60, 65, 70, 75, 80\}$ °C. Accordingly, the selected T_p and T_r levels covered conditions below, within, and above the measured glass-transition region, consistent with temperature ranges previously investigated for thermally activated FFF-printed PLA [37,38]. The holding-time range of 2–8 min was selected within the broader 1–10 min range previously investigated for FFF-printed PLA [11].

A full factorial design with three seven-level factors would require 343 combinations, which would have been experimentally impractical. A 7×7 Latin-square design was therefore adopted, in which all 49 combinations of T_p and t_{hold} were included, with the seven T_r levels balanced across both factors. Because shape fixity is determined only by T_p and t_{hold}, the design constitutes a complete three-replicate 7×7 factorial for this response. Each condition was evaluated using three independently printed and programmed specimens, yielding a final dataset of $49 \times 3 = 147$ measurements. The replicate-level recovery time, shape fixity ratio, and shape recovery ratio were retained to quantify within-condition variability.

2.5. Exploratory data analysis

An exploratory data analysis was performed to characterise the distribution of each response, the strength of the linear association between factors and responses, and the statistical significance of the main effects and two-way interactions. Descriptive statistics and Pearson correlation coefficients were computed on the original response scales. Following inspection of the response distributions, recovery time was transformed using $\log(1+y)$, where y denotes recovery time, to reduce its pronounced right skewness. The same transformation was used in the surrogate-modelling pipeline. Regression-based analysis of variance (ANOVA) was applied to the full 147-measurement dataset. Models for recovery time and shape recovery ratio included T_p, t_{hold}, T_r, and their two-way interactions, whereas the shape fixity model included only T_p, t_{hold}, and their interaction, consistent with its programming-stage dependence (Section 2.3). Continuous factors were mean-centred at the midpoints of their investigated ranges before forming interaction terms, providing physically relevant reference conditions for the Type-III main-effect tests. Given the interaction-containing model structure, Type-III sums of squares were used to test each main effect while retaining the specified two-way interactions. This was a model-specific choice rather than a general preference over Type-II ANOVA. First-, second-, and third-order polynomial fits were additionally evaluated to characterise nonlinear shape-fixity trends.

Within-condition variability was quantified using the pooled standard deviation of the three replicates across the 49 experimental conditions. These response-specific estimates were also used, where relevant, to assess the sensitivity of knee-point selection to objective scaling.

2.6. Machine learning pipeline

Eight supervised regression models were benchmarked for each response under a unified pipeline. The candidate models were selected to cover commonly used regression families in additive-manufacturing surrogate modelling [26,39] and comprised: a Ridge regression with polynomial-feature expansion of degrees one, two, and three, serving as a response surface methodology (RSM)-equivalent baseline; a Random Forest Regressor; a Gradient Boosting Regressor; an Extreme Gradient Boosting (XGBoost) Regressor; a Support Vector Regression with a radial basis function (RBF) kernel (SVR-RBF); a Multi-Layer Perceptron Regressor (MLP); a Gaussian Process Regressor (GPR) with radial basis function and Matérn ($\nu = 1.5, 2.5$) kernels combined with a white-noise term; and a deep fully connected network implemented in PyTorch, denoted DL-MLP, with two hidden layers of 64 units, hyperbolic-tangent activations, and Adam optimisation. The hyperparameter search spaces for all candidate models are provided in Table S2 in the Supplementary Material.

Inputs were z-score standardised within each training fold, with the resulting parameters applied to the corresponding held-out data [40]. Consistent with Section 2.5, recovery time was modelled in the log-transformed space using $\log(1+y)$ and back-transformed for evaluation. The neural models additionally standardised their targets internally. Shape fixity surrogates used only T_p and t_{hold} as inputs, reflecting the causal structure established in Section 2.3, whereas the recovery time and shape recovery surrogates received all three factors.

To prevent replicate leakage, headline performance was evaluated using nested leave-one-condition-out (LOCO) cross-validation, with all three replicates of one condition held out in each outer fold and hyperparameters selected by condition-grouped three-fold inner cross-validation. This provides a more realistic assessment of generalisation to unseen conditions and reduces model-selection bias and overfitting [41,42]. For comparison, a shuffled 10-fold outer protocol using the same grouped inner tuning procedure was also evaluated to assess the sensitivity of model performance to replicate leakage and outer-fold structure.

LOCO R^2 uncertainty was estimated using 2000 bootstrap resamples at the experimental-condition level. Models within half a standard error of the highest R^2 were treated as tied, and the model with the lowest MAE was selected. Performance was reported from pooled out-of-fold predictions using R^2, the root-mean-square error (RMSE), MAE and α_{20} index, defined as the fraction of predictions within ±20% of the measured value [40,43]. Related tolerance-band indices, such as α_{30}, have also been used in recent engineering machine-learning studies [44].

2.7. Process-window analysis

A continuous process-window analysis was carried out by sweeping the adopted surrogates over a 61×61-point grid in (T_p, T_r) at each of the seven holding-time levels within the experimental envelope. At each grid point, the three predicted responses were assembled into a feasibility vector and filtered by practical screening criteria set at $t_{rec} \leq 10$ s, $R_f \geq 90\%$, and $R_r \geq 90\%$. The resulting feasibility regions were visualised as binary red/green tile grids in (T_p, T_r) space, following the deterministic process-capability-space representation described in [45].

2.8. Multi-objective optimisation via NSGA-II

The Pareto-optimal operating window was identified using NSGA-II implemented in the pymoo library with T_p, t_{hold}, and T_r bounded by the experimental envelope. The optimisation problem was formulated as

$$\begin{aligned} \min_{T_p, t_{hold}, T_r} \quad & \left(\widehat{f}_{t_{rec}}(T_p,\ t_{hold}, T_r),\ -\widehat{f}_{\mathrm{R_f}}(T_p, t_{hold}),\ -\widehat{f}_{\mathrm{R_r}}(T_p, t_{hold}, T_r)\right) \\ s.t. \quad & \widehat{f}_{\mathrm{R_f}}(T_p, t_{hold}) \leqslant 100\% \\ s.t. \quad & \widehat{f}_{\mathrm{R_r}}(T_p, t_{hold}, T_r) \leqslant 100\% \end{aligned} \tag{2}$$

where $\widehat{f}_{t_{rec}}$, $\widehat{f}_{R_f}$, and $\widehat{f}_{R_r}$ are the surrogate predictors selected in Section 2.6 and reported in Section 3.3. Consistent with the shape-memory sequence, the shape fixity predictor was evaluated using only T_p and t_{hold}. The physical upper-bound constraints $R_f \leq 100\%$ and $R_r \leq 100\%$ ensured that the predicted shape fixity and shape recovery ratios remained within their physically meaningful upper bounds.

Each NSGA-II run used a population of 80 individuals over 200 generations, with Latin hypercube initialisation, simulated binary crossover, and polynomial mutation. The optimisation was repeated for ten random seeds. From each seed-specific Pareto front, the three single-objective extrema and two knee-point solutions were extracted. For each operating point, the ten seed-specific solutions were clustered in (T_p, t_{hold}, T_r) space after scaling by the experimental design steps (5 °C for T_p and T_r; 1 min for t_{hold}). Solutions within a scaled Euclidean distance of 0.25 were grouped using single-linkage clustering. The largest cluster was taken as the modal cluster, and its mean ± sample standard deviation was reported as a measure of seed-to-seed algorithmic dispersion.

For the primary knee, all three objectives were expressed in minimisation form and min–max normalised within each seed-specific non-dominated set so that each objective spanned $[0, 1]$. The knee point was then selected as the Pareto solution with the smallest Euclidean distance to the ideal point, corresponding to the origin of the normalised objective space. To assess the sensitivity of knee-point selection to objective scaling, a replicate-variability-scaled knee was also determined. With each Pareto solution written in minimisation form as $\boldsymbol{z}_i = \left(\widehat{f}_{t_{rec,i}}, -\widehat{f}_{R_{f,i}}, -\widehat{f}_{R_{r,i}}\right)$, the objectives were rescaled according to

$$\widetilde{z}_{ij} = \frac{z_{ij} - \min_i z_{ij}}{s_j},\ i_{\mathrm{knee}} = \underset{i}{\mathrm{argmin}} \|\widetilde{\boldsymbol{z}}_i\|_2 \tag{3}$$

where s_j is the pooled within-condition standard deviation of response j. Thus, the deviation of each objective from the best value attained on the corresponding Pareto front was expressed in units of its observed replicate variability.

The surrogates supplied deterministic point predictions, and experimental variability was not propagated through NSGA-II but was characterised separately using pooled within-condition standard deviations, LOCO prediction errors, and seed-to-seed dispersion.

3. Results

3.1. Shape-recovery behaviour

Fig. 2 shows representative final recovered shapes of the 4D-printed PLA specimens for the 49 experimental conditions, with one specimen selected from the three replicates per condition. The images illustrate the differences in the final geometry, while quantitative comparisons are based on recovery time, shape fixity ratio, and shape recovery ratio. The full experimental matrix corresponding to these conditions is provided in Table S1 in the Supplementary Material.

Although all specimens were programmed into a comparable bent temporary shape, noticeable differences were observed in the recovery time and in the final recovered geometry. Across the 147 measurements, recovery time varied from 3 to 180 s, shape fixity ratio from 86.8 to 100%, and shape recovery ratio from 0.7 to 96.9%, demonstrating a strong influence of the thermomechanical cycle.

Condition 13 recovered in 3 s while maintaining shape fixity and shape recovery ratios of 97.9% and 91.8%, respectively. In contrast, Condition 44 required 97 s and reached only 0.7% shape recovery despite a 99.5% shape fixity ratio. These examples demonstrate that

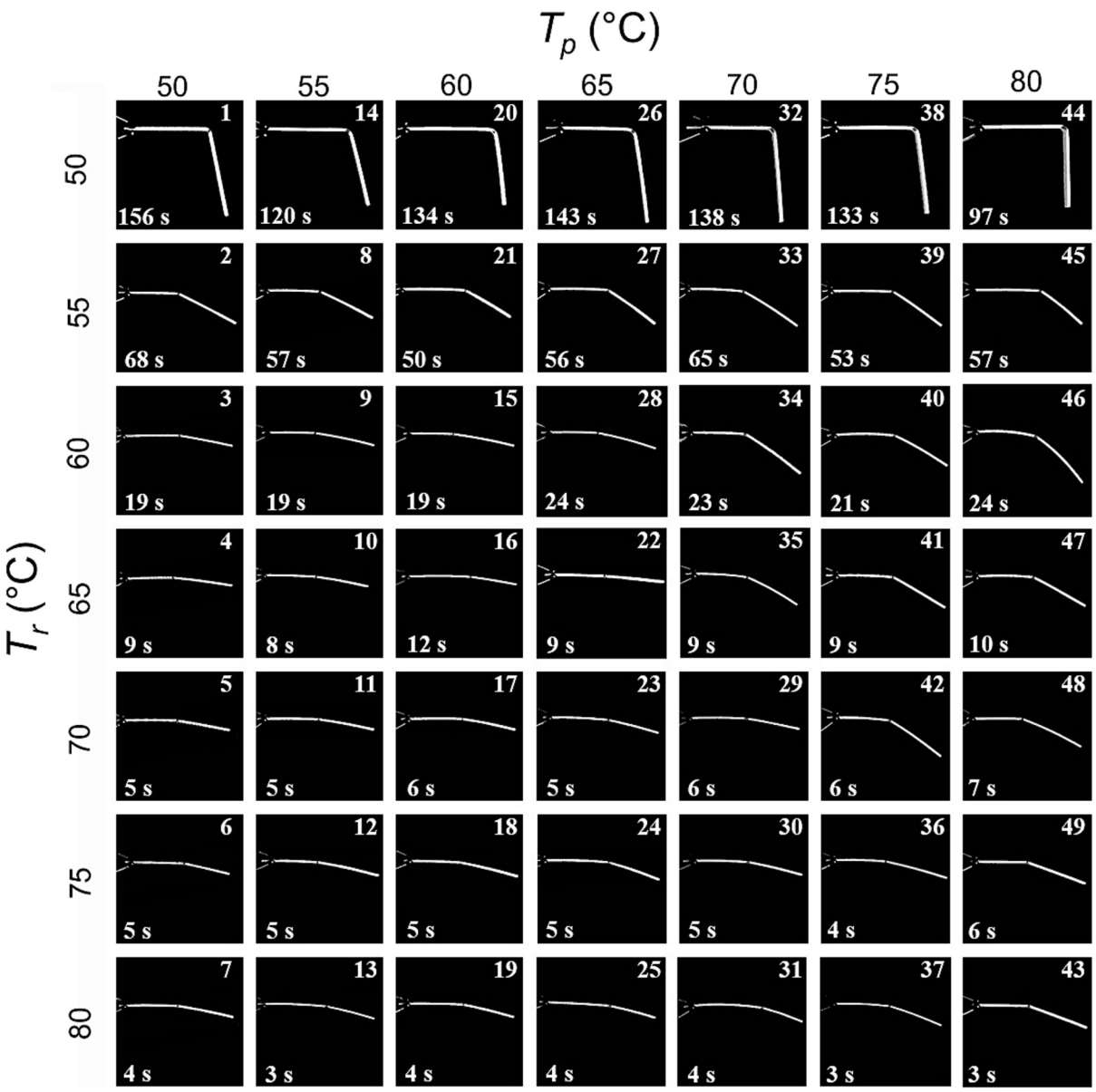


Fig. 2. Representative final recovered shapes for the 49 experimental conditions. Condition numbers and corresponding recovery times are shown at the upper-right and lower-left corners, respectively.

recovery kinetics, temporary-shape fixation, and final recovery are distinct aspects of the shape-memory response.

Accordingly, shape-memory performance cannot be evaluated from recovery time alone: rapid recovery does not necessarily imply high final recovery, and slower recovery may still produce greater return toward the original geometry.

3.2. Descriptive statistics and exploratory analysis

The descriptive statistics confirmed that recovery time exhibited the largest dynamic range (3–180 s, mean 33.3 s, strongly right-skewed), while the shape fixity ratio occupied a narrower band near the top of its scale (86.8–100.0%, mean 97.8%), and the shape recovery ratio spanned almost the full 0–100% envelope (0.7–96.9%, mean 72.6%). The replicate structure further allowed the within-condition variability of these responses to be quantified, with pooled standard deviations of 6.10 s for recovery time, 0.97 percentage points (pp) for the shape fixity ratio, and 3.53 pp for the shape recovery ratio. The Pearson correlation matrix shown in Fig. 3 highlighted that the recovery temperature showed the strongest linear association with recovery time ($r = -0.805$) and shape recovery ratio ($r = +0.712$), whereas the shape fixity ratio showed a different response, correlating primarily with the programming temperature ($r = +0.661$) and only weakly with the holding time ($r = -0.061$). This is consistent with the causal sequence of the shape-memory cycle, because R_f is determined before the recovery stage and is therefore analysed using T_p and t_{hold} only.

The Type-III ANOVA results are summarised in Table 1. For log-transformed recovery time, all three main effects were significant at the centred reference conditions, and all three two-way interactions were also significant, with recovery temperature showing the largest F-statistics. For the shape fixity ratio, which was modelled using T_p and t_{hold} only, programming temperature was significant, whereas holding time and their interaction were not. The shape recovery ratio showed a strongly coupled response, with all three main effects and all three two-way interactions reaching significance. Because significant interactions were present for recovery time and shape recovery ratio, their main effects are interpreted as conditional effects at the centred reference conditions rather than as global independent effects. The corresponding

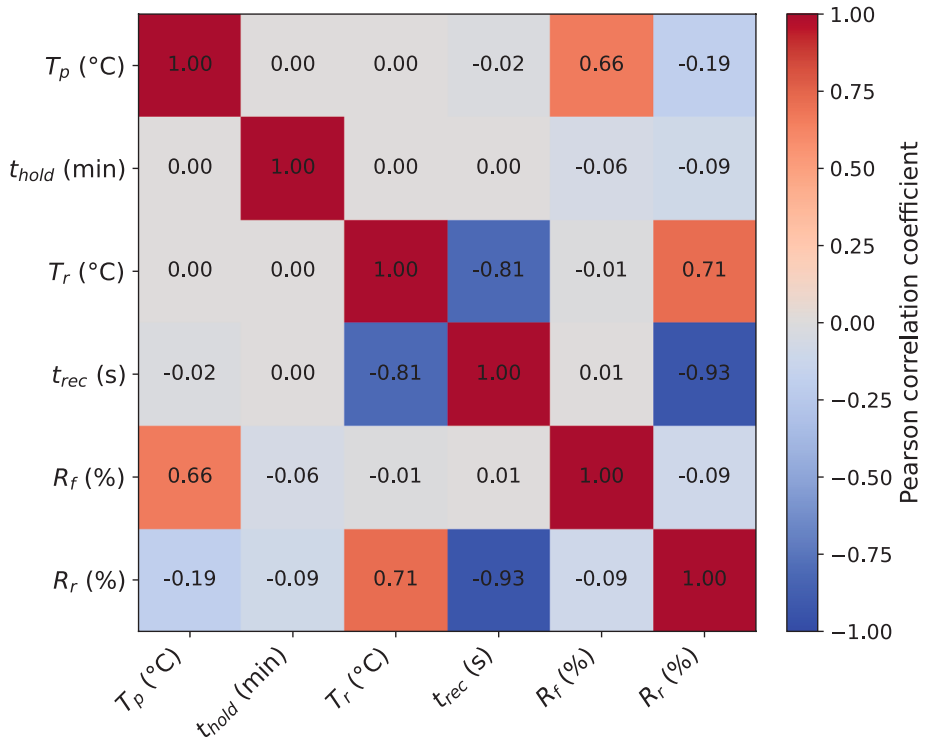


Fig. 3. Pearson correlation matrix between the process factors and functional responses for the 147 measurements.

Table 1
Type-III ANOVA for the mean-centred linear main effects and bilinear two-way interactions. The shape fixity ratio was modelled using T_p and t_{hold} only. Significance: $^*p < 0.05$, $^{**}p < 0.01$, $^{***}p < 0.001$; n.s., not significant.

Response	Term	F	p	
$\log(1+t_{rec})$(model $R^2 = 0.938$)	T_p	6.66	0.0109	*
	t_{hold}	5.54	0.0200	*
	T_r	2022.50	< 0.0001	***
	$T_p \times t_{hold}$	58.20	< 0.0001	***
	$T_p \times T_r$	33.32	< 0.0001	***
	$t_{hold} \times T_r$	28.11	< 0.0001	***
R_f(model $R^2 = 0.441$)	T_p	111.61	< 0.0001	***
	t_{hold}	0.94	0.3340	n.s.
	$T_p \times t_{hold}$	0.27	0.6025	n.s.
R_r(model $R^2 = 0.690$)	T_p	36.37	< 0.0001	***
	t_{hold}	15.12	0.0002	***
	T_r	285.75	< 0.0001	***
	$T_p \times t_{hold}$	60.36	< 0.0001	***
	$T_p \times T_r$	34.62	< 0.0001	***
	$t_{hold} \times T_r$	42.33	< 0.0001	***

model R^2 values were 0.938 for $\log(1+t_{rec})$, 0.441 for the shape fixity ratio, and 0.690 for the shape recovery ratio.

The comparatively lower R^2 of the linear-plus-bilinear model for the shape fixity ratio reflects its pronounced nonlinear response. The marginal response plots in Fig. 4 showed that the shape fixity ratio increased sharply from 90.2% at $T_p = 50$ °C to 98.8% at 55 °C, after which it remained within approximately 98.2–99.7% over the higher programming-temperature levels, while varying only between 97.4% and 98.2% across the holding-time levels. Polynomial fits using T_p alone accounted for 43.6%, 65.4%, and 79.8% of the variance at first, second, and third order, respectively, confirming a pronounced saturation-type response. Once the programming temperature entered the measured glass-transition region of the investigated PLA, the temporary shape was largely fixed, while increasing the holding time produced no statistically significant additional effect. This saturation behaviour motivated the use of more flexible surrogate models for subsequent prediction and optimisation.

3.3. Surrogate benchmarking

The cross-validated R^2 values of the eight candidate surrogates per response are summarised in Table 2 under both the shuffled 10-fold and leave-one-condition-out (LOCO) protocols, while the corresponding bar chart and parity plots are shown in Figs. 5 and 6, respectively. Headline model performance was evaluated using LOCO cross-validation. All three responses were predicted well for held-out conditions. Recovery time achieved a LOCO R^2 of 0.973 (RMSE 7.29 s, MAE 3.58 s), the shape fixity ratio 0.874 (RMSE 1.17 pp, MAE 0.76 pp), and the shape recovery ratio 0.975 (RMSE 4.31 pp, MAE 3.21 pp). For recovery time, all eight candidates achieved $R^2 > 0.94$, indicating consistently strong predictive performance across candidate models.

The comparison between the shuffled and LOCO protocols was used to assess the sensitivity of the reported performance to replicate leakage and associated change in outer-fold structure. The differences were small across the candidate models, with a maximum shuffled to LOCO difference of 0.081 R^2 and differences below 0.030 for the majority of model-response combinations. For the adopted surrogates, the shuffled-to-LOCO differences were 0.004 for recovery time, 0.020 for the shape fixity ratio, and 0.002 for the shape recovery ratio. The leading candidates were therefore largely unchanged between the two evaluation protocols. Nevertheless, condition-grouped LOCO remained the primary evaluation protocol because it assesses each surrogate on factor combinations that were not encountered during training and avoids placing replicate measurements from the same condition in both the training and test partitions.

The leading candidates were separated by differences comparable to the resampling uncertainty of the LOCO R^2. Bootstrap resampling over experimental conditions yielded standard errors of 0.010 for recovery time, 0.068 for the shape fixity ratio, and 0.010 for the shape recovery ratio. For recovery time, the two highest LOCO R^2 values differed by only 0.0002, while the leading shape fixity models were also separated by differences substantially smaller than the corresponding bootstrap

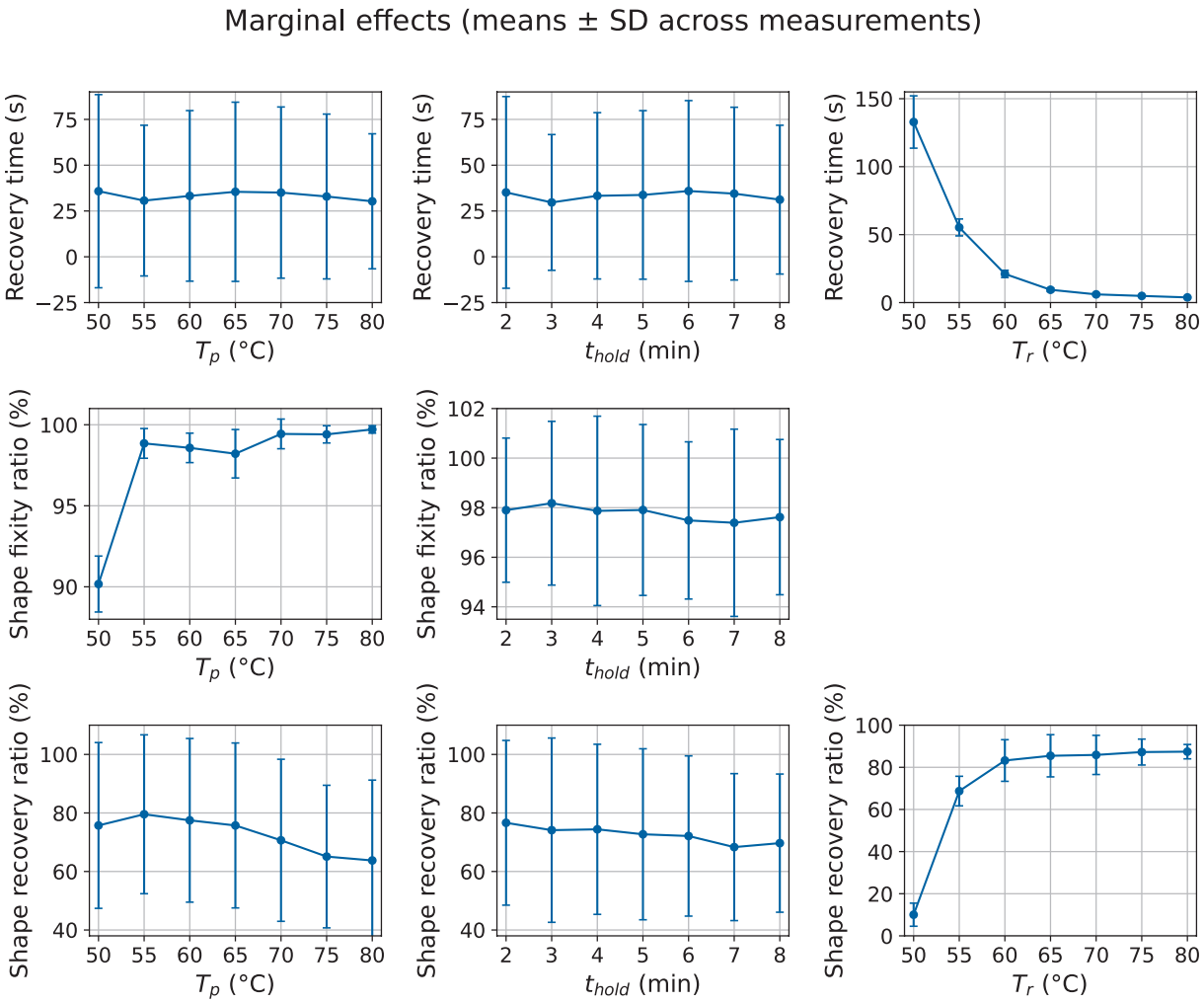


Fig. 4. Marginal response plots of the process factors on recovery time, shape fixity ratio, and shape recovery ratio. Panels are omitted where a factor is not a causal input of the response.

Table 2
Coefficient of determination (R^2) per response and candidate surrogate on the 147-measurement dataset. Each cell reports the shuffled 10-fold value followed by the LOCO value obtained with nested hyperparameter selection. The adopted surrogate for each response is shown in bold.

Model	t_{rec}	R_f	R_r
Ridge-RSM	0.970/0.952	0.777/0.728	0.953/0.919
Random Forest	0.972/0.949	**0.894/0.874**	0.977/0.960
Gradient Boosting	0.971/0.943	0.884/0.859	0.977/0.968
XGBoost	0.973/0.954	0.884/0.846	**0.977/0.975**
SVR-RBF	0.965/0.960	0.861/0.842	0.963/0.882
Gaussian Process	0.974/0.973	0.881/0.830	0.976/0.937
MLP-sklearn	**0.977/0.973**	0.884/0.869	0.968/0.892
DL-MLP (torch)	0.974/0.960	0.879/0.874	0.977/0.919

standard error. For shape fixity ratio, six candidate models fell within the predefined half-standard-error band, indicating that the selected Random Forest should be regarded as one of several statistically comparable high-performing surrogates rather than as a uniquely superior model. Accordingly, selecting the surrogate based solely on the maximum R^2 would have distinguished between models whose performance was effectively tied at the resolution of the resampling analysis. The adopted surrogates were therefore selected using the tie-break rule defined in Section 2.6. Among models lying within half a standard error of the highest LOCO R^2, the model with the lowest MAE was retained. This criterion selected the MLP for recovery time, the Random Forest for the shape fixity ratio, and XGBoost for the shape recovery ratio.

The α_{20} indices of the adopted surrogates were 0.80 for recovery time, 1.00 for the shape fixity ratio, and 0.88 for the shape recovery ratio. The lower α_{20} value for recovery time reflects the strict relative tolerance at the fastest conditions, where ±20% corresponds to an absolute interval of less than 1 s. By contrast, the $\alpha_{20} = 1.00$ obtained for the shape fixity ratio reflects the combination of its narrow response range and the relatively broad ±20% acceptance band, rather than implying zero prediction error. The parity plots in Fig. 6 therefore include the $y = 1.2x$ and $y = 0.8x$ reference lines used to define this index, while the error metrics and input structures of the adopted surrogates are summarised in Table 3.

3.4. Process-window analysis

The grid sweep over the experimental envelope revealed a feasibility region $(t_{rec} \leq 10s, R_f \geq 90\%, R_r \geq 90\%)$ strongly concentrated at high recovery temperatures. Fig. 7 visualises the surrogate-predicted feasibility regions in the (T_p, T_r) space at all seven investigated holding-time levels. The feasible fraction of the grid generally decreased with increasing holding time, from 36.9% at $t_{hold} = 2$ min to 29.3%, 16.3%, 15.6%, and 12.5% at 3, 4, 5, and 6 min respectively. No grid point satisfied all three screening criteria at 7 min, whereas a narrow feasible region reappeared at 8 min, covering 1.6% of the grid.

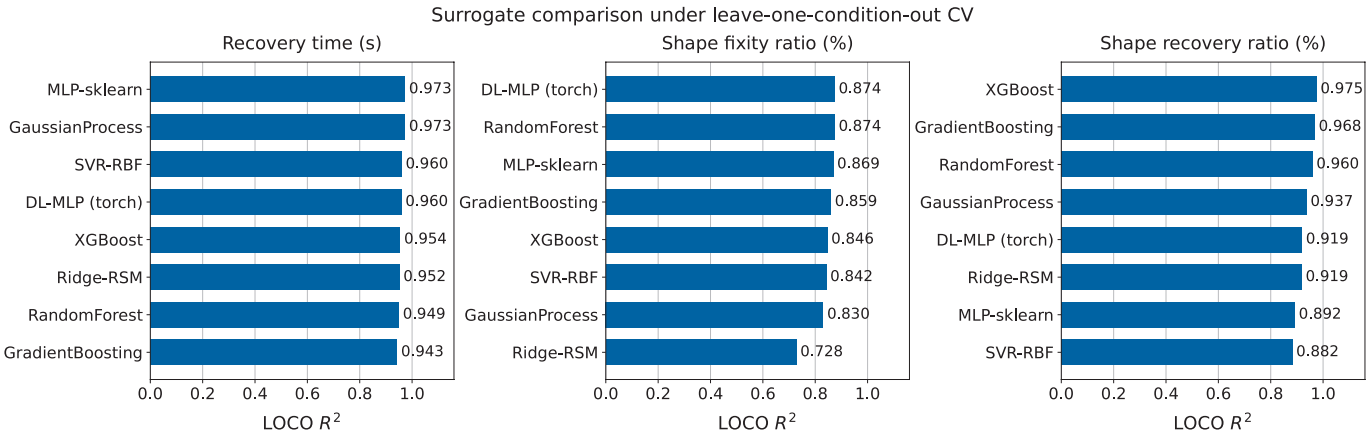


Fig. 5. Cross-validated coefficients of determination of the eight candidate surrogates under the LOCO evaluation protocol.

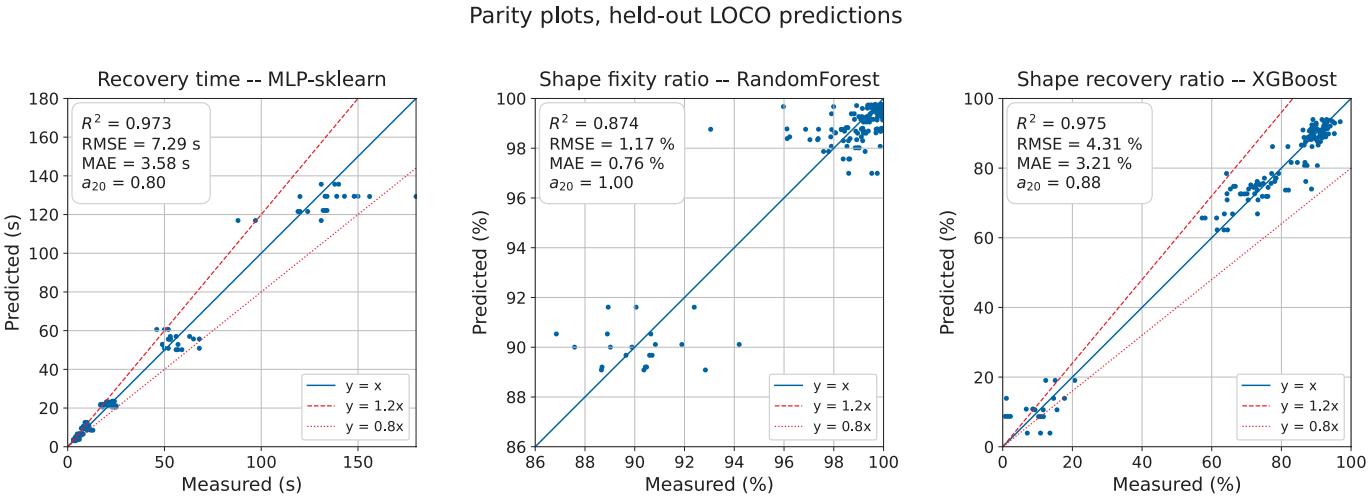


Fig. 6. Parity plots of the adopted per-response surrogates on the LOCO held-out folds. Dashed and dotted lines mark the $y = 1.2x$ and $y = 0.8x$ bounds of the α_{20} index.

Table 3
Adopted surrogate for each response, corresponding input variables, LOCO cross-validated R^2, RMSE, MAE, and α_{20} index.

Response	Surrogate	Inputs	R^2	RMSE	MAE	α_{20}
t_{rec}	MLP-sklearn	T_p, t_{hold}, T_r	0.973	7.29 s	3.58 s	0.80
R_f	Random Forest	T_p, t_{hold}	0.874	1.17 pp	0.76 pp	1.00
R_r	XGBoost	T_p, t_{hold}, T_r	0.975	4.31 pp	3.21 pp	0.88

The shape recovery ratio was the limiting response at the longest holding times. At $t_{hold} = 7$ min, its maximum predicted value over the (T_p, T_r) grid was 89.5%, marginally below the 90% screening criterion whereas at 8 min the maximum predicted value increased to 90.3%. A similar weak non-monotonic tendency was also observed in the experimental data, where the mean shape recovery ratio decreased from 72.1% at 6 min to 68.3% at 7 min and increased slightly to 69.7% at 8 min. Given the small magnitude of these differences, the reappearance of a narrow feasible region at 8 min should not be interpreted as evidence of a distinct change in material behaviour.

3.5. Pareto front and knee-point operating window

The NSGA-II runs produced a three-dimensional Pareto front in (t_{rec}, R_f, R_r) space, with one representative front shown in Fig. 8 and the corresponding pairwise projections in Fig. 9. Across the seed runs, the non-dominated sets contained approximately 17–22 solutions and spanned recovery times of 2.81–4.41 s, shape fixity ratios of 98.48–99.82%, and shape recovery ratios of 72.48–98.59%. All non-dominated solutions were located at relatively high recovery temperatures ($T_r \geq 72.5$ °C), with most occurring near the upper end of the investigated recovery-temperature range. This high T_r concentration was consistent with the favourable region identified by the process-window screening in Section 3.4.

The knee point, defined as the Pareto solution closest to the ideal point in the min–max-normalised objective space, was located at $T_p = 67.543 \pm 0.046$ °C, $t_{hold} = 2.000 \pm 0.001$ min, and $T_r = 79.998 \pm 0.005$ °C, with predicted responses of $t_{rec} = 3.136 \pm 0.002$ s, $R_f = 99.719\% \pm < 0.001\%$, and $R_r = 91.702 \pm 0\%$. Nine of the ten seed-specific solutions belonged to the modal cluster, with only minor dispersion within this operating-point neighbourhood.

To assess the sensitivity of knee-point selection to objective scaling, a replicate-variability-scaled criterion defined in Section 2.8 was also applied. The resulting knee was located at $T_p = 53.548 \pm 0.086$ °C, $t_{hold} = 3.004 \pm 0.005$ min, and $T_r = 80.000$ °C, with predicted responses of $t_{rec} = 3.202 \pm 0.001$ s, $R_f = 99.458 \pm 0\%$, and $R_r = 94.757 \pm 0\%$. All ten seed-specific solutions belonged to the same modal cluster. Relative to the min–max knee, this operating point increased the predicted recovery time by approximately 0.07 s and reduced R_f by 0.26 pp, while increasing R_r by 3.06 pp.

The two knee criteria therefore produced similar objective-space

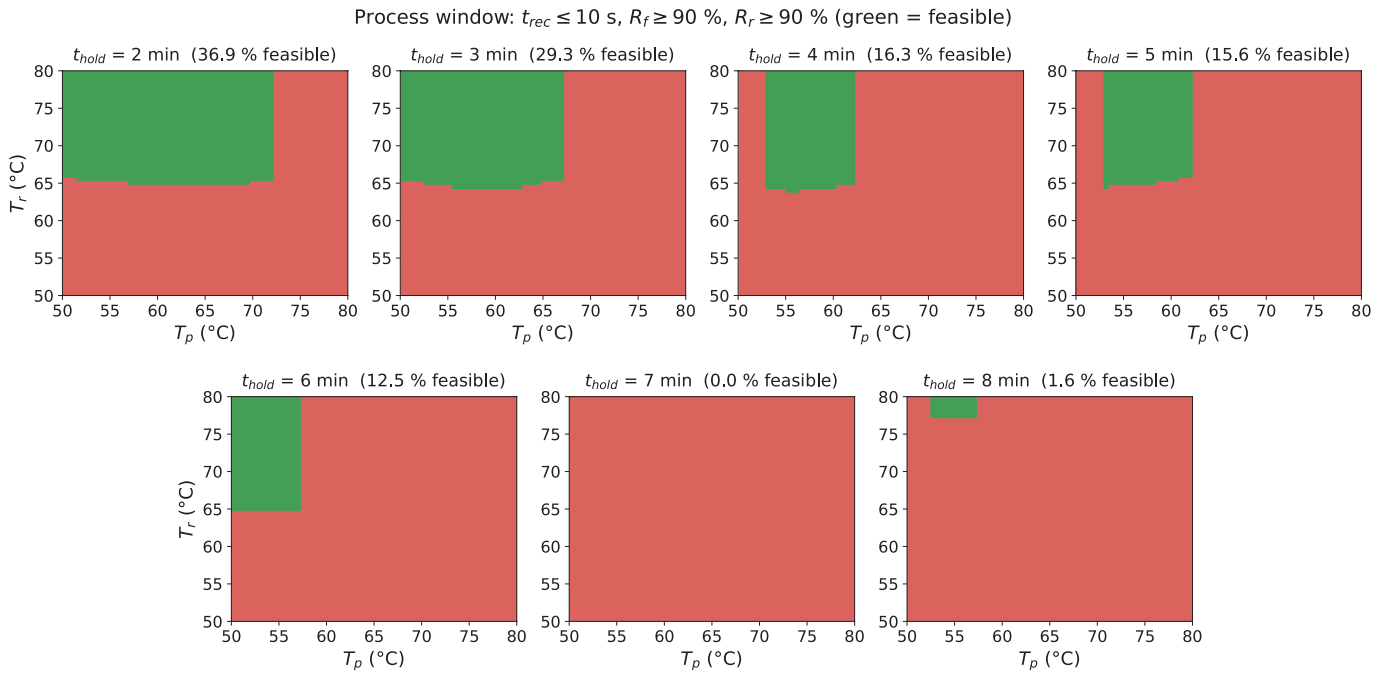


Fig. 7. Binary feasibility maps of the surrogate-predicted process window in (T_p, T_r) space at all seven investigated holding-time levels, with green regions satisfying $t_{rec} \leq 10s, R_f \geq 90\%$, and $R_r \geq 90\%$ simultaneously. (For interpretation of the references to colour in this figure legend, the reader is referred to the web version of this article.)

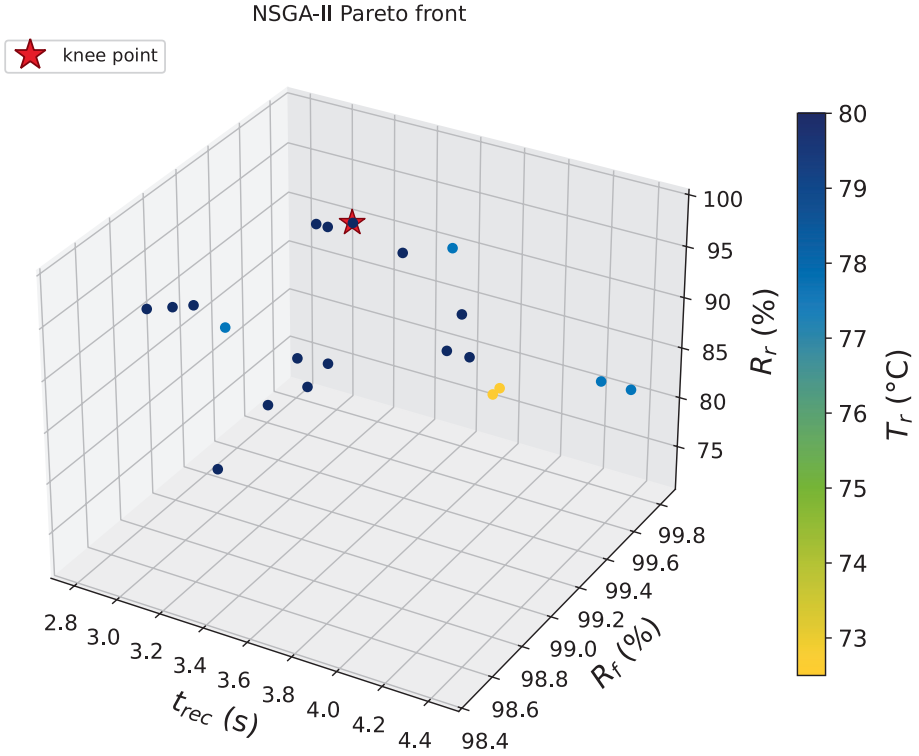


Fig. 8. Three-dimensional Pareto front in (t_{rec}, R_f, R_r) space returned by the NSGA-II search under the physical admissibility constraints $R_f \leq 100\%$ and $R_r \leq 100\%$, with the min–max knee point highlighted.

performance but substantially different operating conditions, particularly in T_p, which differed by approximately 14 °C. The selected operating point is consequently sensitive to the objective-scaling rule even though the resulting trade-off among the three responses remains similar. The min–max knee was retained as the primary operating point because it follows the pre-specified primary selection rule, whereas the replicate-variability-scaled knee is reported as part of the sensitivity analysis.

A compact summary of the optimisation results is provided in Table 4, which reports the three single-objective extrema together with the two knee-point solutions. The single-objective extrema occupied distinct regions of the Pareto front and involved clear trade-offs among

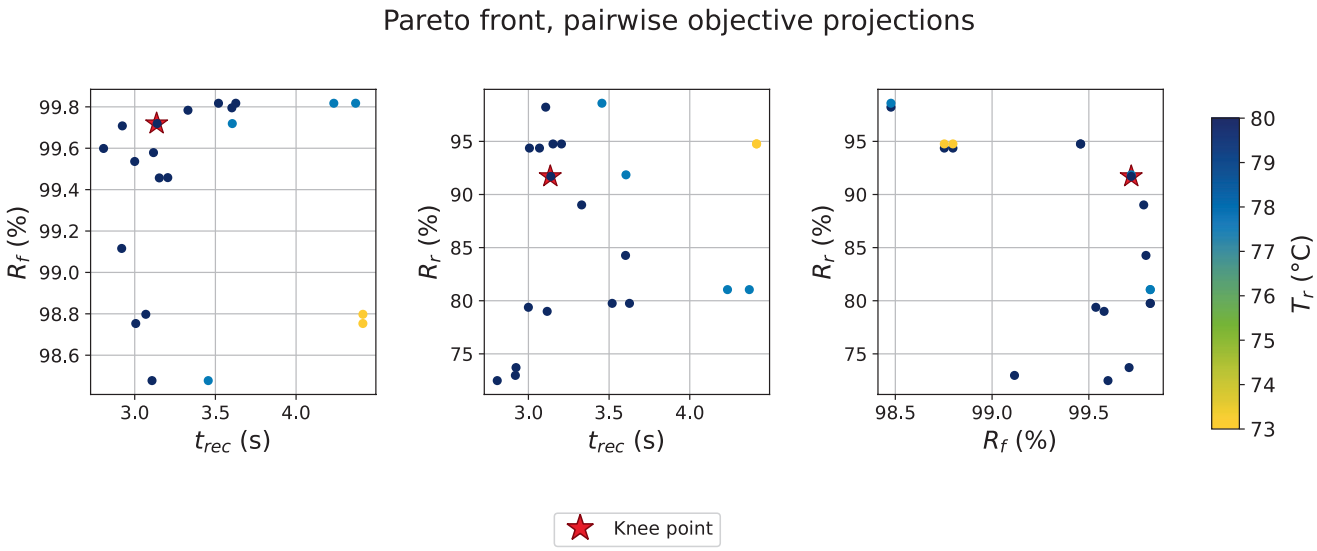


Fig. 9. Pairwise projections of the NSGA-II Pareto front in objective space. Marker colour denotes the recovery temperature, T_r.

Table 4
Representative operating points of the NSGA-II Pareto front. Corresponding statistics calculated over all ten NSGA-II seeds are reported in Table S3 in the Supplementary Material.

Operating point	T_p(°C)	t_{hold}(min)	T_r(°C)	t_{rec}(s)	R_f(%)	R_r(%)	Seeds
Minimum recovery time	77.856± < 0.001	8.000± < 0.001	80.000± < 0.001	2.807± < 0.001	99.599 ± 0	72.483 ± 0	9/10
Maximum shape fixity ratio	77.503 ± 0.002	4.996± < 0.004	80.000± < 0.001	3.626± < 0.001	99.818 ± 0	79.754 ± 0	5/10
Maximum shape recovery ratio	57.493 ± 0.008	2.000± < 0.001	77.498 ± 0.001	3.455± < 0.001	98.477± < 0.001	98.592 ± 0	10/10
Knee point (min–max)	67.543 ± 0.046	2.000± < 0.001	79.998 ± 0.005	3.136 ± 0.002	99.719± < 0.001	91.702 ± 0	9/10
Knee point (replicate-variability-scaled)	53.548 ± 0.086	3.004 ± 0.005	80.000± < 0.001	3.202 ± 0.001	99.458 ± 0	94.757 ± 0	10/10

recovery time, shape fixity ratio, and shape recovery ratio. Relative to the min–max knee, the minimum-recovery-time solution reduced t_{rec} by 0.33 s but decreased R_r by 19.22 pp; the maximum-shape-fixity solution increased R_f by only 0.10 pp while decreasing R_r by 11.95 pp; and the maximum-shape-recovery solution increased R_r by 6.89 pp at the expense of 0.32 s in recovery time and 1.24 pp in shape fixity. These results quantify the trade-off structure represented by the Pareto front.

3.6. Experimental validation

The optimisation-derived operating points were experimentally assessed using independently printed and programmed specimens. For practical implementation, the setpoints were rounded to controllable values: (78 °C, 8.0 min, 80 °C) for minimum recovery time, (78 °C, 5.0 min, 80 °C) for maximum shape fixity, (57 °C, 2.0 min, 77 °C) for maximum shape recovery, (68 °C, 2.0 min, 80 °C) for the min–max knee, and (54 °C, 3.0 min, 80 °C) for the replicate-variability-scaled knee. At each operating point, three specimens were independently printed and programmed, and all three functional responses were measured using the same protocol as the main experimental campaign. Across the five validation points, the measured recovery time ranged from 2.91 ± 0.03 to 3.71 ± 0.12 s, the shape fixity ratio from 97.73 ± 0.72 to 99.57 ± 0.59%, and the shape recovery ratio from 72.30 ± 2.01 to 96.68 ± 1.68%. Fig. 10 compares the measured means ± standard deviation with the corresponding optimisation predictions reported in Section 3.5. The complete mean ± standard deviation results for all validation operating points are also reported in Table S4 in the Supplementary Material.

Overall, the validation experiments reproduced the predicted

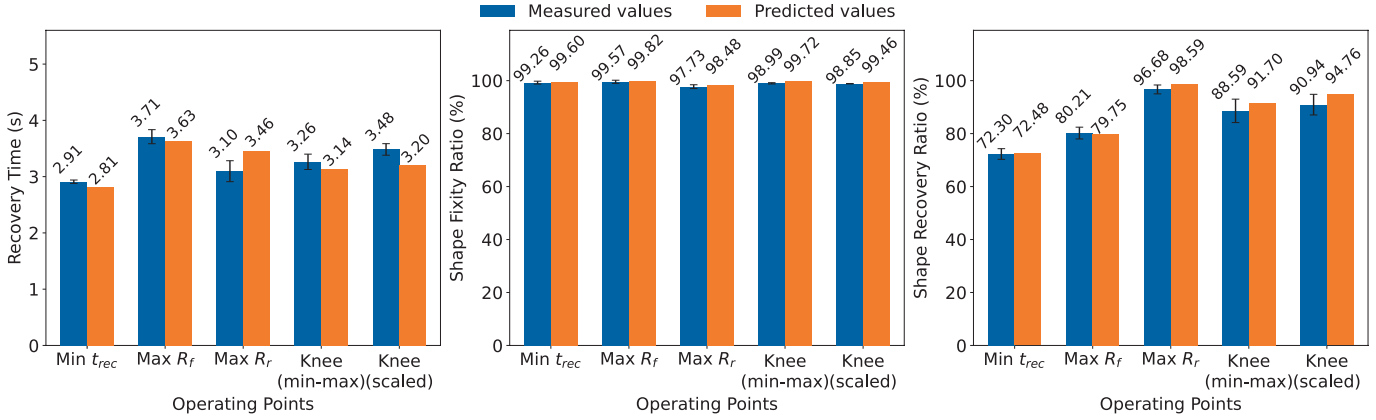


Fig. 10. Comparison of the optimisation-predicted and experimentally measured responses at the five validation operating points; "Knee (scaled)" denotes the replicate-variability-scaled knee.

response trends of the selected operating points. The three single-objective solutions retained their intended response characteristics, while both knee solutions provided rapid recovery and high shape fixity. The replicate-variability-scaled knee also shifted the experimental trade-off towards greater final shape recovery relative to the primary min–max knee.

4. Discussion

4.1. Thermomechanical control of the shape-memory response

The present results consistently show that the recovery temperature, T_r, is the dominant thermomechanical parameter controlling the recovery kinetics and final shape recovery of 4D-printed PLA. This conclusion is supported by the exploratory analysis, process-window maps, and the NSGA-II Pareto search, which concentrated favourable solutions at high T_r. This behaviour agrees well with the thermal activation mechanism of thermally responsive shape-memory polymers, where recovery is triggered when heating above the switching transition restores segmental mobility and allows the stored elastic driving force to return the material toward its permanent shape [3,46]. The DSC analysis of the investigated filament identified a glass-transition region of approximately 55–65 °C. Accordingly, recovery above this region provides greater molecular mobility and promotes more rapid and extensive recovery, whereas recovery near or below the transition region remains kinetically restricted [37]. The present findings remain consistent with previous FFF-printed PLA studies showing that recovery or activation temperature strongly governs shape-recovery kinetics [37,38].

Programming conditions showed a different role. Shape fixity increased sharply between 50 and 55 °C and subsequently approached a saturated level, while holding time had no significant additional effect on shape fixity. This trend is consistent with the increase in segmental mobility near the transition region required for deformation and temporary-shape fixation [3,47]. However, higher programming temperatures did not necessarily improve subsequent recovery. Previous studies similarly reported reduced shape recovery at higher deformation temperatures, attributed to lower storage modulus and reduced internal stress generated during programming [37]. Thus, once shape fixation is saturated, increasing t_{hold} provides little additional benefit to R_f, while its influence on recovery remains interaction dependent.

The process-window analysis reflected the same coupled behaviour. The feasibility region generally contracts with increasing holding time, and shape recovery becomes the limiting response at longer durations. The disappearance of the feasibility region at 7 min and its narrow reappearance at 8 min is better interpreted as a threshold-crossing effect, potentially influenced by local surrogate behaviour near the upper boundary of the investigated holding-time range, rather than as evidence of a distinct change in material behaviour. The corresponding maximum predicted recovery ratios differed by only 0.8 pp (89.5% at 7 min and 90.3% at 8 min), which is small relative to the pooled within-condition variability of R_r (3.53 pp). Overall, a high recovery temperature favoured rapid and high recovery, while favourable shape-memory performance depended on the combined programming and recovery history rather than on any single parameter [37,38,47].

4.2. Surrogate reliability and model selection

The exploratory regression analysis revealed nonlinear and interaction-dependent response behaviour, supporting the use of flexible surrogate models for process-window mapping and optimisation [27,35]. This was especially relevant for the shape fixity ratio, whose saturation-type response was not well represented by the linear-plus-bilinear model $\left(R^2 = 0.441\right)$. The ANOVA and surrogate-model results should therefore be viewed as complementary rather than directly comparable, as they involve different model structures and evaluation procedures.

Under LOCO cross-validation, the adopted surrogates achieved R^2 values of 0.973, 0.874, and 0.975 for recovery time, shape fixity ratio, and shape recovery ratio, respectively. The comparatively lower R^2 for shape fixity reflects its narrow response range and saturation behaviour rather than poor predictive accuracy, as indicated by its RMSE of 1.17 pp and MAE of 0.76 pp. The differences among the leading models were also comparable to or smaller than the bootstrap uncertainty of the LOCO R^2; for shape fixity, six candidates fell within the predefined half-standard-error band. The selected Random Forest should therefore be regarded as one of several statistically comparable high-performing surrogates, supporting the predefined MAE-based tie-break rule rather than selection solely by the maximum cross-validated score. Although shuffled cross-validation generally produced slightly higher scores, the differences from LOCO were below 0.030 for most model-response combinations and the rankings remained largely unchanged. Because LOCO excludes all replicates of the held-out condition from training, it prevents condition-level information leakage, analogous to grouped validation in repeated-measures data [48]. The close agreement between shuffled and LOCO performance therefore indicates that the high predictive performance was not primarily driven by replicate leakage, but by the ability of the surrogate models to capture systematic nonlinear relationships within the investigated domain. Accordingly, these results support reliable prediction at held-out conditions within the investigated thermomechanical domain, but not extrapolation beyond it.

4.3. Multi-objective optimisation

The NSGA-II search confirmed that recovery time, shape fixity ratio, and shape recovery ratio are competing objectives, demonstrating that overall shape-memory performance cannot be represented by a single-response criterion. The practical relevance of these trade-offs was evident from the single-objective extrema: relative to the primary knee, a 0.33 s reduction in recovery time was accompanied by a 19.22 pp decrease in shape recovery ratio, whereas a gain of only 0.10 pp in shape fixity ratio resulted in an 11.95 pp decrease in shape recovery ratio. These contrasts highlight the value of selecting a compromise solution rather than optimising any single response in isolation.

Both the process-window analysis and the NSGA-II consistently favoured the high-T_r region, although they serve different purposes. The process-window analysis identifies a broader feasible region based on predefined thresholds [45], whereas NSGA-II defines the Pareto trade-off set from which a compromise operating point is selected. Two knee criteria were therefore examined. Although both produced similar objective-space performance, they selected different programming conditions, with programming temperatures differing by approximately 14 °C. This sensitivity indicates that the final operating point depends on how the competing objectives are scaled and prioritised [49] and should therefore be interpreted as one favourable compromise within a Pareto-optimal region rather than as a uniquely defined optimum.

Independent experimental validation supported the practical reliability of the selected Pareto operating points. The measured responses remained close to the optimisation predictions, and the single-objective solutions retained their intended response characteristics. Both knee solutions also remained rapid, high-fixity compromises, while the replicate-variability-scaled knee shifted the trade-off towards greater final shape recovery, consistent with the optimisation results.

4.4. Limitations

The Latin-square design did not sample every three-factor combination, so some optimiser-selected conditions represent interpolations within a non-uniformly sampled experimental domain. Predictions may therefore be less reliable in sparsely sampled regions and near the domain boundaries, which motivated independent experimental

validation of the selected operating points.

The optimisation also relies on deterministic surrogate predictions, with experimental variability considered in the replicate-variability-scaled knee-selection criterion but not propagated through NSGA-II. LOCO performance therefore supports interpolation within the investigated domain rather than extrapolation beyond it. In addition, the stepwise nature of the tree-based surrogates may limit the smooth representation of continuous response relationships [50]. Accordingly, the selected settings should be interpreted as favourable operating regions rather than infinitely precise optima.

Finally, the conclusions are specific to the investigated PLA, factor ranges, and printing conditions. Material formulation and experimental protocol may alter programming behaviour [11,37], while holding-time effects at durations shorter than the investigated 2–8 min range remain unresolved. Variations in printing conditions may also modify thermal history and residual stress, thereby affecting shape fixation and recovery [38,51].

5. Conclusion

This study presented an integrated framework combining structured experiments, machine-learning surrogates, process-window analysis, and NSGA-II for multi-objective optimisation of thermomechanical programming in 4D-printed PLA. The main findings are as follows:

i. Recovery temperature, T_r, was the dominant parameter governing recovery behaviour, with both the feasibility analysis and the Pareto solutions consistently favouring the high-T_r region.
ii. Shape fixity ratio increased sharply from 90.2% at $T_p = 50$ °C to 98.8% at 55 °C and subsequently approached a plateau, while holding time showed no significant additional effect on shape fixity ratio within the investigated range.
iii. The adopted surrogate models achieved LOCO R^2 values of 0.973, 0.874, and 0.975 for recovery time, shape fixity ratio, and shape recovery ratio, respectively, supporting strong predictive performance at held-out conditions within the investigated thermomechanical domain.
iv. The NSGA-II confirmed clear trade-offs among the three responses, with the selected knee depending on objective scaling. Experimental validation at five operating points supported the optimisation results, with maximum absolute deviations of 0.36 s, 0.75 pp, and 3.82 pp for recovery time, shape fixity ratio, and shape recovery ratio, respectively.

These results highlight the value of integrating experimental design, supervised machine learning, process-window analysis, and evolutionary multi-objective optimisation for the systematic characterisation of shape-memory programming and recovery in 4D-printed PLA. The framework is intended for within-domain, offline programming optimisation and provides a transferable methodology rather than a universal set of PLA programming parameters. In practical use, it can serve as an offline decision-support and process-planning tool for identifying suitable programming and recovery conditions before deployment, thereby reducing the need for extensive trial-and-error experimentation. Future work should extend the framework by (i) incorporating broader classes of material systems, including polymer blends, bilayer architectures, and multi-material structures, within a unified surrogate modelling framework; (ii) coupling the offline operating-window recommendations with closed-loop or learning-based actuation strategies to enable adaptation to environmental disturbances during operation [52,53]; and (iii) directly sampling the neighbourhood of the identified knee region to reduce reliance on interpolation and support uncertainty-aware surrogate models that propagate experimental variability through the optimisation process.

CRediT authorship contribution statement

Ayhan Hacıoğlu: Writing – original draft, Visualization, Validation, Supervision, Methodology, Investigation, Data curation, Conceptualization. **Meltem Eryildiz:** Writing – review & editing, Writing – original draft, Visualization, Validation, Methodology, Investigation, Data curation, Conceptualization. **Erkan Caner Ozkat:** Writing – review & editing, Writing – original draft, Visualization, Methodology, Formal analysis, Conceptualization.

Declaration of competing interest

The authors declare that they have no known competing financial interests or personal relationships that could have appeared to influence the work reported in this paper.

Acknowledgments

This study has been supported by the Recep Tayyip Erdoğan University Development Foundation (Grant number: 020260080020538).

Appendix A. Supplementary data

Supplementary data to this article can be found online at https://doi.org/10.1016/j.matdes.2026.117160.

Data availability

Data will be made available on request.

References

[1] L. Chang, T. Read, Plastic deformation and diffusionless phase changes in metals—the gold-cadmium beta phase, JOM 3 (1) (1951) 47–52, https://doi.org/10.1007/BF03398954.
[2] W.J. Buehler, J.V. Gilfrich, R.C. Wiley, Effect of low-temperature phase changes on the mechanical properties of alloys near composition TiNi, J. Appl. Phys. 34 (5) (1963) 1475–1477, https://doi.org/10.1063/1.1729603.
[3] A. Lendlein, S. Kelch, Shape-memory polymers, Angew. Chem. Int. Ed. 41 (12) (2002) 2034–2057, https://doi.org/10.1002/1521-3773(20020617)41:12<2034::AID-ANIE2034>3.0.CO;2-M.
[4] A.A. Fetisova, M.A. Surmeneva, R.A. Surmenev, Advanced design concepts for shape-memory polymers in biomedical applications and soft robotics, Polymers 18 (2) (2026) 214, https://doi.org/10.3390/polym18020214.
[5] S. Valvez, P.N. Reis, L. Susmel, F. Berto, Fused filament fabrication-4d-printed shape memory polymers: a review, Polymers 13 (5) (2021) 701, https://doi.org/10.3390/polym13050701.
[6] J. Li, Z. Liang, T. Li, Q. Wan, X. Huang, Q. Kan, A comprehensive review on 4d printing and applications of thermo-induced shape memory polymers, Int. J. Smart Nano Mater. 16 (1) (2025) 24–83, https://doi.org/10.1080/19475411.2025.2458833.
[7] Z. Lyu, J. Wang, Y. Chen, 4d printing: interdisciplinary integration of smart materials, structural design, and new functionality, Int. J. Extreme Manuf. 5 (3) (2023) 032011, https://doi.org/10.1088/2631-7990/ace090.
[8] S. Olhan, B. Antil, P. Maimí, B. Behera, Advances in 4d printing of polymeric composite smart materials, Compos. Struct. (2025) 119859, https://doi.org/10.1016/j.compstruct.2025.119859.
[9] M. Lalegani Dezaki, A. Zolfagharian, F. Demoly, M. Bodaghi, Human–material interaction enabled by fused filament fabrication 4d printing, Adv. Eng. Mater. 26 (7) (2024) 2301917, https://doi.org/10.1002/adem.202301917.
[10] M. Enriconi, R. Rodriguez, M. Araújo, J. Rocha, R. García-Martín, J. Ribeiro, J. Pisonero, M. Rodríguez-Martín, A comprehensive review of fused filament fabrication. Numerical modeling approaches and emerging trends, Appl. Sci. 15 (12) (2025) 6696, https://doi.org/10.3390/app15126696.
[11] M. Eryildiz, Influence of process parameters on the shape recovery properties of 4d-printed polylactic acid parts produced by fused deposition modeling, J. Mater. Eng. Perform. 32 (9) (2023) 4258–4269, https://doi.org/10.1007/s11665-023-07946-x.
[12] M. Eryildiz, Development and fabrication of 3d-printed foam-filled pla/pcl lattice structures with tunable shape memory and mechanical performance, Polym. Eng. Sci. 66 (1) (2026) 595–607, https://doi.org/10.1002/pen.70243.
[13] S.S. Kumar, J.S. Akmal, M. Salmi, 4d printing of shape memory polymer with continuous carbon fiber, Prog. Addit. Manuf. 9 (6) (2024) 1985–1995, https://doi.org/10.1007/s40964-023-00553-1.

[14] Q. Ge, A.H. Sakhaei, H. Lee, C.K. Dunn, N.X. Fang, M.L. Dunn, Multimaterial 4d printing with tailorable shape memory polymers, Sci. Rep. 6 (1) (2016) 31110, https://doi.org/10.1038/srep31110.
[15] K. Sudan, K. Kate, D. Popa, R. Sarabia-Riquelme, P. Ajjarapu, V. Ramesh, W. Meadows, Design, characterization and shape recovery behavior of 3d/4d printed shape memory polymers (smps), Prog. Addit. Manuf. 11 (1) (2026) 1065–1080, https://doi.org/10.1007/s40964-025-01397-7.
[16] M. Shadman, H. Ahmadi, D. Rahmatabadi, M. Seidi, Study on the shape memory performance of 4d-printed auxetic cellular structures with energy absorption application, Macromol. Mater. Eng. 311 (2) (2026) e00320, https://doi.org/10.1002/mame.202500320.
[17] A.N. Altunkaya, E.C. Ozkat, M. Avci, Analytical-to-ai pipeline: Modeling and optimization of entropy generation in pulsating non-newtonian heat flow, Comput. Math. Appl. 205 (2026) 195–211, https://doi.org/10.1016/j.camwa.2025.12.021.
[18] E.C. Ozkat, Laser beam welding state classification: a deep learning framework for acoustic signal intelligence, Machines 14 (6) (2026) 652, https://doi.org/10.3390/machines14060652.
[19] N. Korkmaz Can, E.C. Ozkat, N. Ceryan, S. Ceryan, Benchmarking ml approaches for earthquake-induced soil liquefaction classification, Appl. Sci. 15 (21) (2025) 11512, https://doi.org/10.3390/app152111512.
[20] E.C. Ozkat, Photodiode signal patterns: unsupervised learning for laser weld defect analysis, Processes 13 (1) (2025) 121, https://doi.org/10.3390/pr13010121.
[21] A.T. Tasdemir, E.C. Ozkat, G.Y. Ozkat, F. Gul, Linking tea aroma chemistry to quality grades via a single mos gas sensor: classical machine learning vs. deep learning, Sensors 26 (12) (2026), https://doi.org/10.3390/s26123877.
[22] J. Zhao, H. Nguyen, T. Nguyen-Thoi, P.G. Asteris, J. Zhou, Improved Levenberg–Marquardt backpropagation neural network by particle swarm and whale optimization algorithms to predict the deflection of RC beams, Eng. Comput. 38 (Suppl 5) (2022) 3847–3869, https://doi.org/10.1007/s00366-020-01267-6.
[23] S. Ghani, S.C. Sapkota, R.K. Singh, A. Bardhan, P.G. Asteris, Modelling and validation of liquefaction potential index of fine-grained soils using ensemble learning paradigms, Soil Dyn. Earthq. Eng. 177 (2024) 108399, https://doi.org/10.1016/j.soildyn.2023.108399.
[24] A. Benzaamia, M. Ghrici, R. Rebouh, N. Zygouris, P.G. Asteris, Predicting the shear strength of rectangular RC beams strengthened with externally-bonded FRP composites using constrained monotonic neural networks, Eng. Struct. 313 (2024) 118192, https://doi.org/10.1016/j.engstruct.2024.118192.
[25] A. Benzaamia, M. Ghrici, R. Rebouh, A.A. Ghrici, P.G. Asteris, Prediction of chloride resistance level in concrete using optimized tree-based machine learning models, Bull. Comput. Intell. 1 (1) (2025) 104–117, https://doi.org/10.53941/bci.2025.100007.
[26] K.Y. Gyabaah, B. Mahoney, A.K. Martey, C. Yan, P. Mensah, G. Li, Machine learning-assisted polymer and polymer composite design for additive manufacturing, AI Materials 1 (1) (2026) 2, https://doi.org/10.3390/aimater1010002.
[27] M.d.C. Cesario, M.C. Pereira, L.E.B.d. Souza, G.C.d.S. Moraes, M.B. Francisco, J.L. J. Pereira, Explainable machine learning and multi-objective optimization for pet-cf15 fused filament fabrication process design, Int. J. Adv. Manuf. Technol. 143 (9) (2026) 5377–5397, https://doi.org/10.1007/s00170-026-17838-8.
[28] Z. Xu, S. Zhang, X. Sun, S. Mao, R. Xiao, Machine learning-assisted inverse design of 3d shape morphing in liquid crystal elastomer composite strips, Adv. Funct. Mater. 36 (29) (2026) e26924, https://doi.org/10.1002/adfm.202526924.
[29] S. Lee, S. Kang, J. Nam, J. Yu, M. Kim, S. Ryu, Inverse design of thermally active composite via policy-transferred reinforcement learning, Mater. Horiz. (2026), https://doi.org/10.1039/d6mh00239k.
[30] D. Rahmatabadi, M. Aberoumand, K. Soltanmohammadi, E. Soleyman, I. Ghasemi, M. Baniassadi, K. Abrinia, M. Bodaghi, M. Baghani, Influence of programming and recovery parameters on compressive behaviors of 4d-printed biocompatible polyvinyl chloride or vinyl–poly (ε-caprolactone) blends, Adv. Eng. Mater. 26 (12) (2024) 2400301, https://doi.org/10.1002/adem.202400301.
[31] M.L. Dezaki, M. Bodaghi, 4d printing and programming of continuous fibre-reinforced shape memory polymer composites, Eur. Polym. J. 210 (2024) 112988, https://doi.org/10.1016/j.eurpolymj.2024.112988.
[32] K. Mirasadi, D. Rahmatabadi, I. Ghasemi, M. Khodaei, M. Banias-sadi, M. Bodaghi, M. Baghani, 3d and 4d printing of petg–abs–fe3o4 nanocomposites with supreme remotely driven magneto-thermal shape-memory performance, Polymers 16 (10) (2024) 1398, https://doi.org/10.3390/polym16101398.
[33] D. Rahmatabadi, M. Khajepour, A. Bayati, K. Mirasadi, M.A. Yousefi, A. Shegeft, I. Ghasemi, M. Baniassadi, K. Abrinia, M. Bodaghi, et al., Advancing sustainable shape memory polymers through 4d printing of polylactic acid-polybutylene adipate terephthalate blends, Eur. Polym. J. 216 (2024) 113289, https://doi.org/10.1016/j.eurpolymj.2024.113289.
[34] C. Zheng, X. Li, J. Tan, A. Tan, X. Li, H. Ni, W. Yu, Y. Bai, P. Hu, W.M. Huang, et al., Cold crystallization-enabled permanent shape transformation in 4d-printed pla/tpu composites for personalized wearable devices, Chem. Eng. J. (2025) 167141, https://doi.org/10.1016/j.cej.2025.167141.
[35] A. Forrester, A. Sobester, A. Keane, in: Engineering Design Via Surrogate Modelling: A Practical Guide, John Wiley & Sons, 2008, https://doi.org/10.1002/9780470770801.
[36] K. Giannoukou, S. Marelli, B. Sudret, Uncertainty-aware multifidelity surrogate modeling with noisy data, ASCE-ASME J. Risk Uncertainty Eng. Syst. Part A: Civ. Eng. 11 (3) (2025) 04025037, https://doi.org/10.1061/AJRUA6.RUENG-1441.
[37] W. Wu, W. Ye, Z. Wu, P. Geng, Y. Wang, J. Zhao, Influence of layer thickness, raster angle, deformation temperature and recovery temperature on the shape-memory effect of 3d-printed polylactic acid samples, Materials 10 (8) (2017) 970, https://doi.org/10.3390/ma10080970.
[38] M. Barletta, A. Gisario, M. Mehrpouya, 4d printing of shape memory polylactic acid (pla) components: investigating the role of the operational parameters in fused deposition modelling (fdm), J. Manuf. Process. 61 (2021) 473–480, https://doi.org/10.1016/j.jmapro.2020.11.036.
[39] C. Tian, T. Li, J. Bustillos, S. Bhattacharya, T. Turnham, J. Yeo, A. Moridi, Data-driven approaches toward smarter additive manufacturing, Adv. Intell. Syst. 3 (12) (2021) 2100014, https://doi.org/10.1002/aisy.202100014.
[40] P.G. Asteris, T. Sivenas, M. Gkantou, A. Formisano, T.T. Le, Estimation of axial load-carrying capacity of elliptical concrete filled steel tubular columns using computational intelligence, J. Build. Eng. 112 (2025) 113738, https://doi.org/10.1016/j.jobe.2025.113738.
[41] P.G. Asteris, A.D. Skentou, A. Bardhan, P. Samui, K. Pilakoutas, Predicting concrete compressive strength using hybrid ensembling of surrogate machine learning models, Cem. Concr. Res. 145 (2021) 106449, https://doi.org/10.1016/j.cemconres.2021.106449.
[42] D.J. Armaghani, P.G. Asteris, A comparative study of ANN and ANFIS models for the prediction of cement-based mortar materials compressive strength, Neural Comput. Appl. 33 (2021) 4501–4532, https://doi.org/10.1007/s00521-020-05244-4.
[43] P.G. Asteris, K.D. Tsavdaridis, M.E. Lemonis, F.P.V. Ferreira, T.T. Le, C.J. Gantes, A. Formisano, AI-powered GUI for prediction of axial compression capacity in concrete-filled steel tube columns, Neural Comput. Appl. 36 (2024) 22429–22459, https://doi.org/10.1007/s00521-024-10405-w.
[44] F. Bendriss, Z. Harichane, A.D. Skentou, R. Rebouh, A.A. Ghrici, P.G. Asteris, Advanced machine learning models for estimating seismic bearing capacity of shallow strip footings considering P- and S-wave effects, Soil Dyn. Earthq. Eng. 200 Part B (2026) 109853, https://doi.org/10.1016/j.soildyn.2025.109853.
[45] E.C. Ozkat, P. Franciosa, D. Ceglarek, Laser dimpling process parameters selection and optimization using surrogate-driven process capability space, Opt. Laser Technol. 93 (2017) 149–164, https://doi.org/10.1016/j.optlastec.2017.02.012.
[46] T. Dayyoub, A.V. Maksimkin, O.V. Filippova, V.V. Tcherdyntsev, D.V. Telyshev, Shape memory polymers as smart materials: a review, Polymers 14 (17) (2022) 3511, https://doi.org/10.3390/polym14173511.
[47] K. Yu, Q. Ge, H. Qi, Reduced time as a unified parameter determining fixity and free recovery of shape memory polymers, Nat. Commun. 5 (2014) 3066, https://doi.org/10.1038/ncomms4066.
[48] A. Karbalaie, F. Abtahi, C.K. Häger, Participant-aware model validation for repeated-measures data: comparative cross-validation study, JMIR AI 5 (2026) e87728, https://doi.org/10.2196/87728.
[49] L. He, H. Ishibuchi, A. Trivedi, H. Wang, Y. Nan, D. Srinivasan, A survey of normalization methods in multiobjective evolutionary algorithms, IEEE Trans. Evol. Comput. 25 (6) (2021) 1028–1048, https://doi.org/10.1109/TEVC.2021.3076514.
[50] L.M. Meijerink, E. Schuit, K.G.M. Moons, A.M. Leeuwenberg, Plug-and-play use of tree-based methods: consequences for clinical prediction modeling, J. Clin. Epidemiol. 184 (2025) 111834, https://doi.org/10.1016/j.jclinepi.2025.111834.
[51] P. Wu, T. Yu, M. Chen, D. Hui, Effect of printing speed and part geometry on the self-deformation behaviors of 4D printed shape memory PLA using FDM, J. Manuf. Process. 84 (2022) 1507–1518, https://doi.org/10.1016/j.jmapro.2022.11.007.
[52] Q. Ji, M. Chen, C. Zhao, X. Zhang, X.V. Wang, L. Wang, L. Feng, Feedback control for the precise shape morphing of 4d-printed shape memory polymer, IEEE Trans. Ind. Electron. 68 (12) (2020) 12698–12707, https://doi.org/10.1109/TIE.2020.3040668.
[53] Q. Ji, M. Chen, X.V. Wang, L. Wang, L. Feng, Optimal shape morphing control of 4d printed shape memory polymer based on reinforcement learning, Rob. Comput. Integr. Manuf. 73 (2022) 102209, https://doi.org/10.1016/j.rcim.2021.102209.